ACS Energy LETTERS

http://pubs.acs.org/journal/aelccp

Prussian Blue Analogue Framework Hosts for Li–S Batteries

Dasol Jin, Mihail R. Krumov, Ruth M. Mandel, Phillip J. Milner, and Héctor D. Abruña*

Cite This: *ACS Energy Lett.* 2024, 9, 5822–5829

Read Online

ACCESS | Metrics & More | Article Recommendations | Supporting Information

ABSTRACT: **Lithium–sulfur (Li–S) batteries hold promise for next-generation energy storage due to their high theoretical energy density (~2600 Wh kg^{-1}). However, practical use is hindered by capacity loss from the polysulfide shuttle effect and poor energy efficiency due to slow kinetics. To overcome these challenges, we developed a novel sulfur host material featuring highly porous concave nanocubes derived from a Prussian blue analogue. By controlling the annealing conditions, we achieved a high surface area (up to 248 m^2 g^{-1}), which enhances polysulfide adsorption, thereby reducing sulfur dissolution and minimizing the loss of cathode capacity during cycling. *Operando* Raman spectroscopy revealed that this material also provides a synergistic catalytic effect, lowering polarization/overpotentials within Li–S cells. The optimized material enables an extended battery life with high sulfur loading, a low E/S ratio, and excellent capacity retention over long-term cycles, demonstrating its potential to improve Li–S battery performance.**

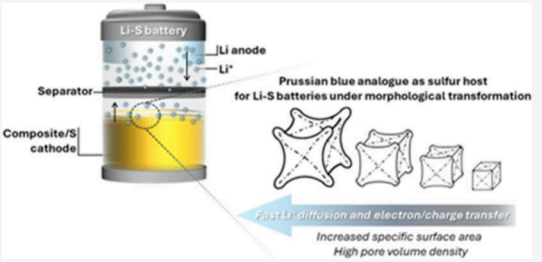

Lithium-sulfur (Li–S) batteries are promising for electric vehicles and smart grids due to their high theoretical capacity (1675 mAh g^{-1}) and energy density (2567 Wh kg^{-1}).[1−3] However, practical challenges like polysulfide dissolution, leading to self-discharge and material loss, and slow charge transfer rates, causing overpotentials and reduced energy efficiency, limit their use. To address these challenges, significant efforts have been directed toward improving the physicochemical properties of the cathode to effectively anchor the sulfur particles, soluble intermediates, and final discharge products.[4−6] While carbon nanomaterials with engineered pores show potential, they often suffer from capacity deterioration due to weak interactions with polar polysulfides.[7,8] In this respect, recent research has focused on chemically trapping or catalytically reducing polysulfides using polar and conductive materials,[9] including metal oxides,[10] metal chalcogenides,[11] and heteroatom doping (e.g., N,[12] O,[13] S,[14] and P[15]). Prussian blue analogues, recognized for their uniform porosity and crystalline structure, are attracting interest in energy storage.[16−20] Their Fe^{2+}/Fe^{3+} framework, connected by cyanide bridges, forms open channels that enhance ion insertion, resulting in stable capacities and improved cycling performance.[21] Materials with high porosity, particularly those with a porous morphology, are crucial for facilitating the transport of Li ions (Li^+). This study investigates how annealing-induced morphological changes in Prussian blue analogues, made using potassium hexacyanoferrate ($K_4Fe(CN)_6$) and cobalt nitrate ($Co(NO_3)_2$), affect the Li–S battery efficiency (Figure S1). The materials, labeled PB@*t*, were fabricated by varying the annealing time (*t*).

As shown in SEM images (Figure 1a–d and Figure S2) all Prussian blue analogue frameworks maintain a consistent cubic shape with high purity and uniformity. Specifically, PB@0.2h features sharp-edged nanocubes, while longer annealing times produce concave structures with protruding corners and inward-curving faces. The average edge lengths decrease in the order PB@0.2h (121 ± 6.7 nm), PB@1h (105 ± 5.2 nm), PB@3h (99 ± 2.5 nm), and PB@6h (95 ± 3.1 nm), indicating that the size reduction and formation of concave structures depend on the annealing time at 400 °C. Transmission electron microscopy (TEM) images (Figure S3) also reveal that increasing annealing time transforms the sulfur host materials, enhancing their porous and concave features. These features are crucial for accommodating high sulfur loading and preserving the structural integrity to mitigate the volume expansion induced by sulfur during electrochemical reaction.[22] To evaluate the porosity of the nanomaterials, N_2 adsorption/desorption measurements were conducted at 77 K (Figure S4), and the results were analyzed by using the Brunauer–Emmett–Teller (BET) method (Figure S5). The BET surface

Received: October 16, 2024
Accepted: November 6, 2024
Published: November 11, 2024

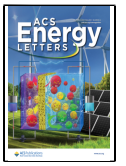

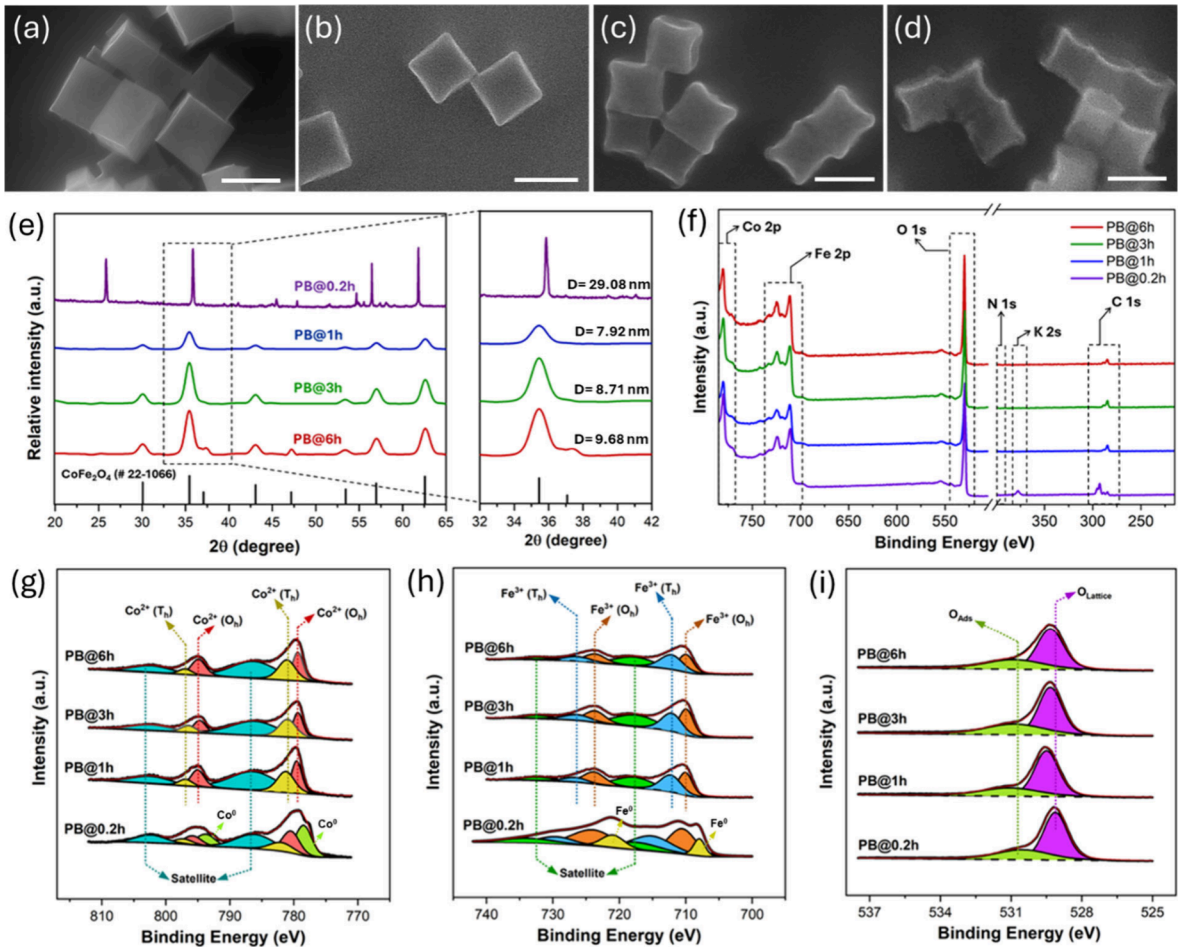

Figure 1. Physicochemical characterization of PB@*t* (*t* = 0.2, 1, 3, and 6h) sulfur hosts. FE-SEM images of (a) PB@0.2h, (b) PB@1h, (c) PB@3h, and (d) PB@6h (scale bar = 100 nm). (e) XRD patterns with partially magnified patterns in the range from 32° to 42°. (f) Survey XPS spectra. High-resolution XPS spectra of (g) Co 2p, (h) Fe 2p, and (i) O 1s regions.

areas increased with annealing time: 55.88 $m^2\ g^{-1}$ for PB@1h, 167.17 $m^2\ g^{-1}$ for PB@3h, and 248.05 $m^2\ g^{-1}$ for PB@6h. PB@6h exhibited a narrow micropore distribution centered at 1.2 nm and a high pore volume of 0.115 $cm^3\ g^{-1}$, while PB@0.2h was nearly nonporous. This demonstrates that longer annealing times increase the surface area and improve micropore distribution, which could enhance electrolyte infiltration and charge transfer, both of which are crucial for sulfur chemistry in Li−S batteries.

X-ray diffraction (XRD) patterns of PB@*t*, shown in Figure 1e, reveal that samples annealed for more than 1h are fully converted to $CoFe_2O_4$ (JCPDS no. 22-1066).[23] In contrast, the PB@0.2h sample, with a shorter annealing time, matches the pristine Prussian blue analogue (JCPDS no. 73-0687).[24,25] Notably, longer annealing times reduce the full width at half-maximum (fwhm) of the diffraction peaks and increase the average crystallite size from 7.92 to 9.68 nm, indicating improved crystalline lattice formation. TEM analysis also shows that PB@6h has clear lattice fringes with a *d*-spacing of 0.25 nm, corresponding to the (311) plane of $CoFe_2O_4$, indicating the formation of a highly crystalline structure during the annealing process (Figure S6a). Additionally, TEM-EDX mapping in Figure S6b confirmed that the elements in the samples were homogeneously blended. Energy dispersive X-ray spectroscopy (EDX) analysis (Figure S7 and Table S1) and ICP-OES analysis (Table S2) were further conducted to confirm the elemental distribution across the entire PB@*t* series. Both analyses showed no significant discrepancies between the samples, demonstrating the precise control over composition achieved by our synthetic method. The sulfur composite state of PB@6h (i.e., PB@6h-S) was examined to verify the uniform distribution of sulfur throughout the entire cathode. EDX results (Figure S8a) confirm the presence of S, Fe, Co, and O in the cathode material, indicating a uniform sulfur loading. XRD analysis (Figure S8b) further confirmed the crystal structure of the PB@6h-S composite, verifying the successful synthesis of a cathode with a uniform sulfur distribution. The peak at around 35.4°, corresponding to the (311) plane of $CoFe_2O_4$, indicates the good crystallinity of the host material.

X-ray photoelectron spectroscopy (XPS) was used to determine the elemental compositions and valence states of the frameworks. The survey spectra in Figure 1f detected C, Co, Fe, and O, while PB@0.2h showed residual K and N due to incomplete precursor decomposition. In the Co 2p region (Figure 1g), peaks at 780.01/795.22 eV and 781.56/796.52 eV, corresponding to Co^{2+} at octahedral (O_h) and tetrahedral (T_h) sites,[26] were commonly observed in PB@*t* (*t* = 1h, 3h, and 6h). Additional satellite peaks at 786.82 and 802.71 eV further confirmed the presence of Co^{2+}.[27] However, the PB@0.2h sample showed extra peaks for metallic Co,[28] likely due to the oxidation of incomplete ferrous ions.[29] The Fe 2p spectra in

https://doi.org/10.1021/acsenergylett.4c02857
ACS Energy Lett. 2024, 9, 5822−5829

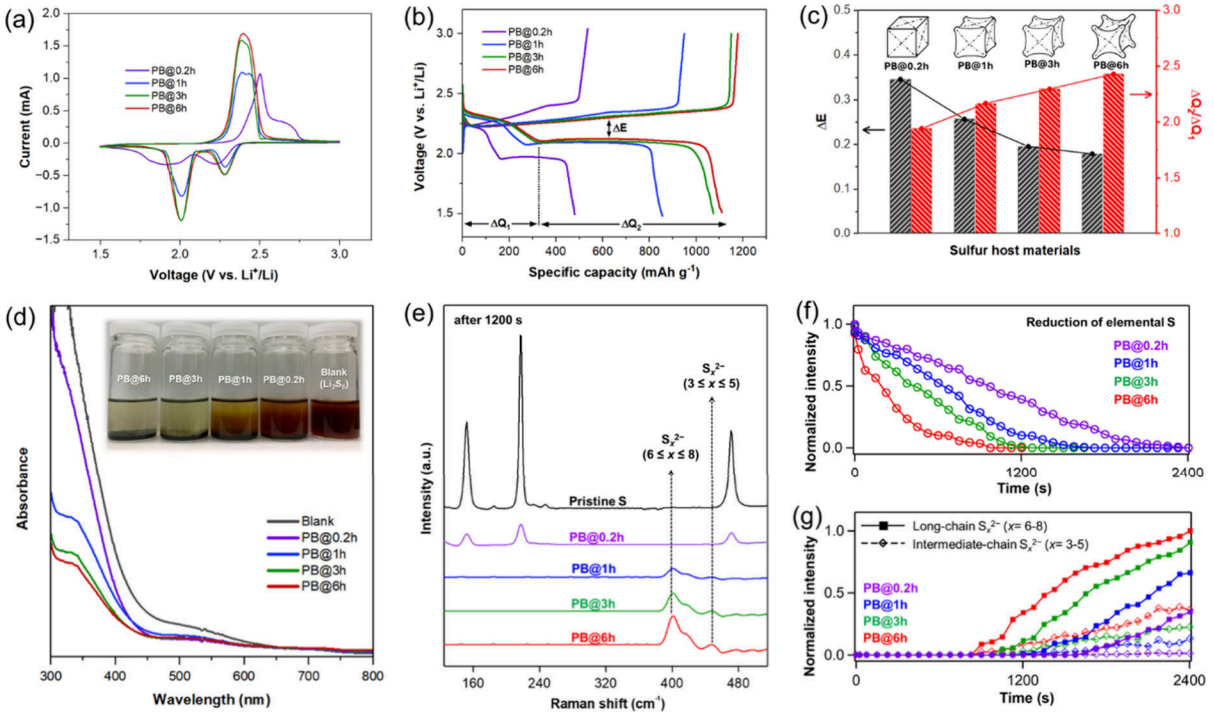

Figure 2. Electrocatalytic enhancement of sulfur redox reactions. (a) CVs of PB@*t* at a scan rate of 0.1 mV s^{-1}. (b) Galvanostatic charge−discharge curves of PB@*t* series-based Li−S batteries at 0.1 C. (c) Plot of ΔE corresponding to 50% state of charge and $\Delta Q_2/\Delta Q_1$ values obtained from the curves in (b). (d) UV/vis absorption spectra of Li_2S_6 solution. (e) Comparison of *operando* Raman intensities across various cathode materials after 1200 s at 2.25 V. Quantified evolution in Raman intensities for (f) S_8 and (g) long-chain and intermediate-chain polysulfides at 2.25 V for 2400 s, respectively. Note that Raman peaks corresponding to S_8 at 218 cm^{-1} and long-chain polysulfides (S_x^{2-}, $6 \le x \le 8$) at 397 cm^{-1} were utilized for normalizing the intensities.

Figure 1h revealed peaks at 710.55/723.17 eV and 713.10/726.50 eV, attributed to Fe^{3+} at O_h and T_h sites,[30] respectively, with satellite peaks at 718.33 and 732.73 eV.[31] However, the PB@0.2h sample exhibited additional peaks corresponding to lower oxidation states of Fe, consistent with the presence of metallic Co observed in the Co 2p region. Note that PB@0.2h, with the shortest annealing time in the series, may exhibit Fe-CN-Co coordination, which alters the electron density at the catalytic metal sites. This is influenced by the electron-withdrawing groups, causing a shift in the binding energy. The O 1s spectra shown in Figure 1e reveal peaks around 529 eV, corresponding to crystal lattice oxygen ($O_{Lattice}$); additionally, a peak near 531 eV may be associated with surface defects, impurities, or chemisorbed oxygen species (O_{Ads}).[30] As the annealing time increased, XPS results confirmed the redistribution of metal ions within the PB@*t* samples, evolving toward a single-phase cubic $CoFe_2O_4$ structure as observed in the XRD patterns (vide supra).

Electrochemical performances of Li−S coin cells with Prussian blue analogue frameworks were assessed by using cyclic voltammetry (CV) and electrochemical impedance spectroscopy (EIS). CV curves in Figure S9 show differing trends in peak currents. For PB@0.2h, synthesized with a short annealing time, the peak currents decreased with cycling. In contrast, the other PB@*t* samples (t = 1, 3, and 6h) maintained their initial peak currents over 5 consecutive cycles, likely due to the absence of any residual Prussian blue precursor in their frameworks. Especially, PB@6h exhibited two distinct reduction peaks at 2.27 and 2.01 V, corresponding to the reduction of sulfur to high-order lithium polysulfides Li_2S_x ($4 \le x \le 8$) and the reduction of LiPSs to solid-state Li_2S_2/Li_2S, respectively, while the measured anodic peak at 2.41 V was attributed to the oxidation of Li_2S_2/Li_2S to S_8.[32] When the initial CV curves were compared (Figure 2a), PB@6h had lower polarization and higher reversibility compared to other samples. To further study the Li−S battery kinetics using PB@*t* materials as sulfur hosts, Tafel slopes were calculated (Figure S10). PB@0.2h, with the shortest annealing time, showed the largest Tafel slope, indicating distinct redox kinetics due to insufficient surface porosity compared to samples annealed at 400 °C for over 1h. Consistent with these results, symmetrical cell testing in Figure S11 confirmed that PB@6h had the highest current magnitude and distinct redox peaks, indicating superior electrocatalytic activity. EIS results (Figure S12) revealed that PB@6h had the smallest semicircle in the Nyquist plot, indicating the lowest charge transfer resistance (R_{ct}) and efficient redox kinetics. After long-term cycling, new semicircles appeared in the midfrequency region, suggesting increased resistance at the electrolyte/electrode interface (R_{surf}).[33,34] PB@6h consistently showed the lowest R_{ct} and R_{surf} values among the frameworks in the series (insets of Figure S12), indicating its superior charge transfer and interfacial stability. Overall, PB@6h demonstrated improved conversion kinetics and performance due to its optimal micropore distribution compared with samples with shorter annealing times. To kinetically investigate this, potentiostatic measurement for Li_2S precipitation were performed as shown in Figure S13a. The calculated Li_2S precipitation capacities were 167.7 mAh g^{-1} for PB@0.2h, 366.4 mAh g^{-1} for PB@1h, 424.0 mAh g^{-1} for PB@3h, and 442.94 mAh g^{-1} for PB@6h, respectively, and the Li_2S nucleation was completed first in the PB@6h electrode, followed by 3, 1, and 0.2h. This suggests

https://doi.org/10.1021/acsenergylett.4c02857
ACS Energy Lett. 2024, 9, 5822−5829

that PB materials with higher porosity can accelerate the reduction of polysulfides. In addition, following the theoretical equations for current−time transients of 4 classical electrochemical deposition methods,[35] dimensionless analysis was also conducted as shown in Figure S13b−e. Li_2S nucleation on PB@0.2h follows a 2D instantaneous deposition (2DI) mode while for the samples with increased annealing duration, the mode transitions to 3D progressive nucleation (3DP), indicating that the nucleation of Li_2S is strongly influenced by the porosity distribution on the catalyst surface. The findings suggest that a higher porosity and micropore distribution in the host material facilitate easier nucleation and growth.

Galvanostatic charge−discharge (GCD) voltage profiles of Li−S cells featuring cathodes based on Prussian blue analogues, with a sulfur loading of 2.1 mg cm^{-2}, are shown in Figure 2b at a rate of 0.1 C (1 C = 1675 mAh g^{-1}). As per the GCD curves, two discharge plateaus and a charging plateau were observed for all sample types: the first discharge plateau corresponds to the reduction of elemental sulfur (S_8) to soluble LiPSs ($S_8 \rightarrow S_8^{2-} \rightarrow S_6^{2-} \rightarrow S_4^{2-}$), while the second plateau reflects the conversion of the intermediate LiPSs to shorter polysulfides and solid state Li_2S_2/Li_2S.[36] The PB@6h exhibited the highest discharge-specific capacity (1110 mAh g^{-1}) when compared to the other samples, specifically, PB@3h (1073 mAh g^{-1}), PB@1h (854 mAh g^{-1}), and PB@0.2h (479 mAh g^{-1}). For a clearer comparison of the catalytic performance across the sample series, the values of voltage difference (ΔE) at 50% state of charge and the catalytic efficiency ($\Delta Q_2/\Delta Q_1$) were plotted in Figure 2c. ΔQ_1 and ΔQ_2 denote the specific capacity of the first and second discharge plateaus: ΔQ_1 reflects/quantifies the quantity of LiPSs generated and potentially diffused to the anode, while ΔQ_2 evaluates the effectiveness of converting LiPSs to Li_2S.[37,38] When the ΔE value is examined, it is evident that PB@0.2h exhibits significantly slower charge transfer kinetics compared to other samples, consistent with the characterizations mentioned above. Notably, among the series of tested nanomaterials, the Li−S cell using PB@6h stands out with the lowest ΔE of 0.17 V and the highest $\Delta Q_2/\Delta Q_1$ ratio of 2.43, highlighting its exceptional catalytic capability in the redox reaction of LiPSs. For comparison, PB@10h was synthesized to determine if increasing the annealing time to 10h would further enhance porosity and concavity. However, SEM (Figure S14a) and TEM (Figure S14b) images showed that the porosity and concavity were similar to those of PB@6h, with some aggregation and clumping observed. The crystalline phase of PB@10h was also nearly identical to that of PB@6h, both showing the $CoFe_2O_4$ spinel phase (Figure S14c). Galvanostatic charging−discharging performances shown in Figure S14d revealed that PB@10h had a specific capacity similar to that of PB@6h but with significantly higher polarization. Therefore, 6-hour annealing process appears optimal for producing well-distributed microporosity without aggregation.

To assess the effectiveness of the nanostructures as sulfur hosts in suppressing the diffusion of lithium polysulfides (LiPSs), we tested their adsorption capacities (Figure 2d). When added to 0.2 M Li_2S_6 solution in DOL/DME (1:1, v/v), PB@6h caused a significant color change from dark orange to colorless, indicating a strong adsorption of LiPSs. In contrast, PB@3h, PB@1h, and PB@0.2h showed less pronounced color changes, in that order. UV−vis spectra further confirm that PB@6h has the lowest absorbance, demonstrating its strong affinity for Li_2S_6. Additionally, as shown in Figure S15, an *in situ* electrochemical study visually confirmed the trapping effect of the PB@*t* series through increased porosity, following the order PB@6h > PB@3h > PB@1h > PB@0.2h. This order was determined by observing the color variation at different depths of the discharging process.

To explore the sulfur redox chemistry, *operando* confocal Raman analyses were conducted through the chronoamperometric measurement (Figures S16 and S17) at an overpotential of ca. 130 mV based on the open-circuit potential (E_{relax} = 2.38 V). Sulfur reduction starts with the breaking of S_8 rings and progresses through steps shortening polysulfides (Li_2S_x), as follows: $x/8\ S_8 \xrightarrow{2e^-}$ long-chain S_x^{2-} $(6 \le x \le 8) \xrightarrow{2e^-}$ intermediate-chain S_x^{2-} $(3 \le x \le 5) \xrightarrow{2e^-}$ short-chain Li_2S_2/LiS_2. Raman spectra taken at the start of discharging showed peaks at 152, 218, and 471 cm^{-1}, indicating elemental sulfur (S_8). As the reduction proceeded, these peaks decreased, and new peaks appeared at 397 cm^{-1} (long-chain polysulfides, S_x^{2-}, $6 \le x \le 8$) and 449 cm^{-1} (intermediate-chain polysulfides, S_x^{2-}, $3 \le x \le 5$). Figure 2e details the transformation from S_8 to polysulfides using different types of sulfur host materials. PB@0.2h showed reduced sulfur intensities with no clear polysulfide peaks, indicating sluggish reduction kinetics, while PB@1h, PB@3h, and PB@6h all displayed strong peaks for long-chain and intermediate-chain polysulfides after 1200 s, especially with PB@6h showing the most intense signals. This suggests that PB@6h promotes faster sulfur conversion, enhancing capacity and reaction kinetics. Figure 2f,g further support this conclusion. In Figure 2f, PB@6h shows the highest sulfur reduction rate at 2.25 V, indicating rapid liquid−solid phase transition kinetics among the samples. Similarly, Figure 2g demonstrates a significant increase in both intermediate- and long-chain polysulfides with PB@6h, highlighting its effectiveness in facilitating polysulfide transformation. In contrast, samples with shorter annealing times exhibit slower kinetics and less effective solid−liquid sulfur reduction, consistent with their lower or nonporous nature as shown by BET analysis. The high porosity of PB@6h enables a more efficient transition from long-chain to intermediate-chain polysulfides compared to the other samples.

Understanding Li^+ transport kinetics is crucial for evaluating battery performance, as charge/discharge processes rely on Li^+ (de)intercalation during electrochemical redox reactions.[39] To assess Li^+ diffusion coefficients (D_{Li^+}), cyclic voltammetry (CV) and galvanostatic intermittent titration technique (GITT) were used. First, by analyzing CV profiles at various scan rates (Figure S18), $D_{Li^+,CV}$ can be calculated using the Randles−Sevcik equation: $I_{peak} = (2.69 \times 10^5) n^{3/2} S D_{Li^+,CV}{}^{1/2} C_{Li^+} * \nu^{1/2}$.[40] The $D_{Li^+,CV}$ values correlate with the slope of I_{peak} vs $\nu^{1/2}$, with PB@6h showing the steepest slopes in the redox reaction regions (anodic peak A and cathodic peaks C1 and C2), indicating superior Li^+ diffusivity compared to other samples (Figure S19). Under the same cell configuration, PB@6h exhibited the highest D_{Li^+} values for each peak, surpassing those of the other samples (Figure S20). In addition, GITT is a widely used method for kinetic analysis that measures transient voltage changes and open-circuit voltage (OCV) under constant current and specific cutoff intervals.[41] Based on Fick's law,[42] this technique assesses Li^+ ion mobility at the electrolyte−electrode interface in Li−S cells. Figure 3a−d presents GITT profiles for Li−S batteries

https://doi.org/10.1021/acsenergylett.4c02857
ACS Energy Lett. 2024, 9, 5822−5829

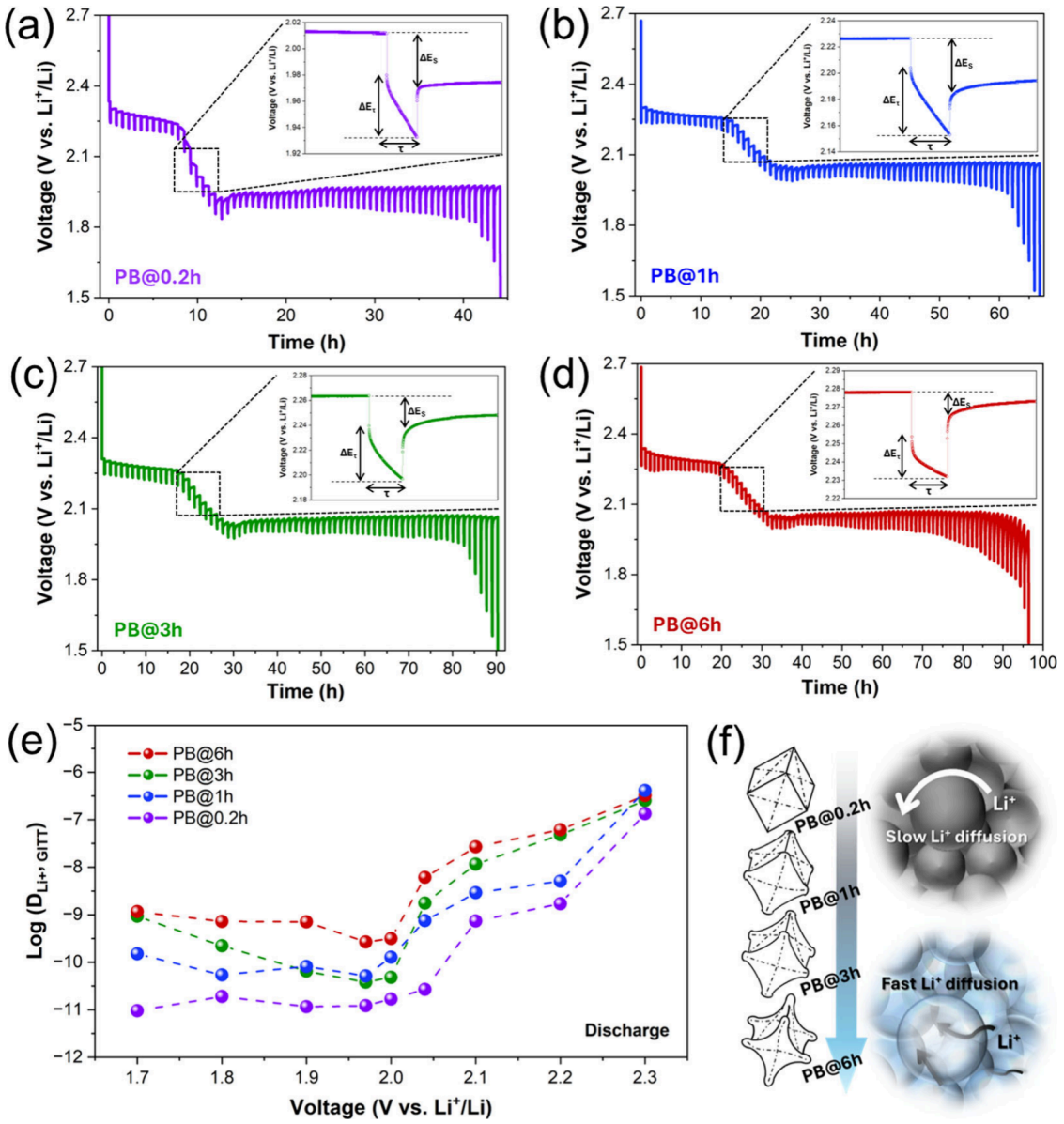

Figure 3. GITT during the initial discharge process of Li−S batteries, employing sulfur cathode materials classified as (a) PB@0.2h, (b) PB@1h, (c) PB@3h, and (d) PB@6h. (e) Comparison of $D_{Li^+,GITT}$ at the specific potentials employed in the GITT measurements depicted in (a−d). For ease of comparison, the calculated D_{Li^+} values derived from both CV and GITT methods are compiled in Table S3. (f) Schematic illustration of diffusion tendencies in the different sample types.

with different sulfur host materials during the first discharge cycle. Figure 3e shows that $D_{Li^+,GITT}$ varies with applied voltage, reflecting a transition between order and disorder in the intercalated species and the hosting materials during electrochemical reactions.[43,44] Among the samples, PB@6h demonstrated the most favorable diffusion properties, indicating superior performance in Li−S batteries. Despite variations in diffusion coefficients across different techniques, D_{Li^+} values consistently rank as PB@6h > PB@3h > PB@1h > PB@0.2h, underscoring the influence of electrode morphology and pore distribution (Figure 3f).

As shown in Figure 4a, Li−S batteries using PB@6h as the sulfur host material demonstrated discharge capacities of 1110, 959, 806, 644, and 510 mAh g^{-1} at rates of 0.1, 0.2, 0.5, 1, and 2 C, respectively, while maintaining a nearly constant polarization difference as the current density increased. During multirate cycling from 0.1 to 2 C, PB@6h demonstrated excellent rate capability, with a reversible capacity of 1015 mAh g^{-1} (94.5% of the initial capacity) when the discharge rate was reduced back to 0.1 C (Figure 4b). For industrial applications, PB@6h cells were tested with sulfur loadings of 2.1, 3.8, and 5.5 mg cm^{-2} (Figure 4c). The cells with 5.5 mg cm^{-2} sulfur loading achieved an areal capacity of 4.11 mAh cm^{-2}, outperforming commercial Li-ion batteries (ca. 4 mAh cm^{-2}).[1] Additionally, PB@6h demonstrated excellent cycling stability over 1000 cycles, with a low capacity fading rate of just 0.05% per cycle at 2 C (Figure S21). Additionally, SEM images of the Li-metal anode after a long-term cycling test revealed a relatively smooth surface devoid of large Li dendrites (Figure S22), indicating the efficacy of polysulfide immobilization in the cathode modified with PB@6h. As shown in Figure 4d, PB@6h retained 76.5% of its initial capacity (3.04 mAh cm^{-2}) after 500 cycles at 0.2 C. Even after 500 cycles, as shown in Figure S23, the PB@6h-S cathodes maintained their structure

https://doi.org/10.1021/acsenergylett.4c02857
ACS Energy Lett. 2024, 9, 5822−5829

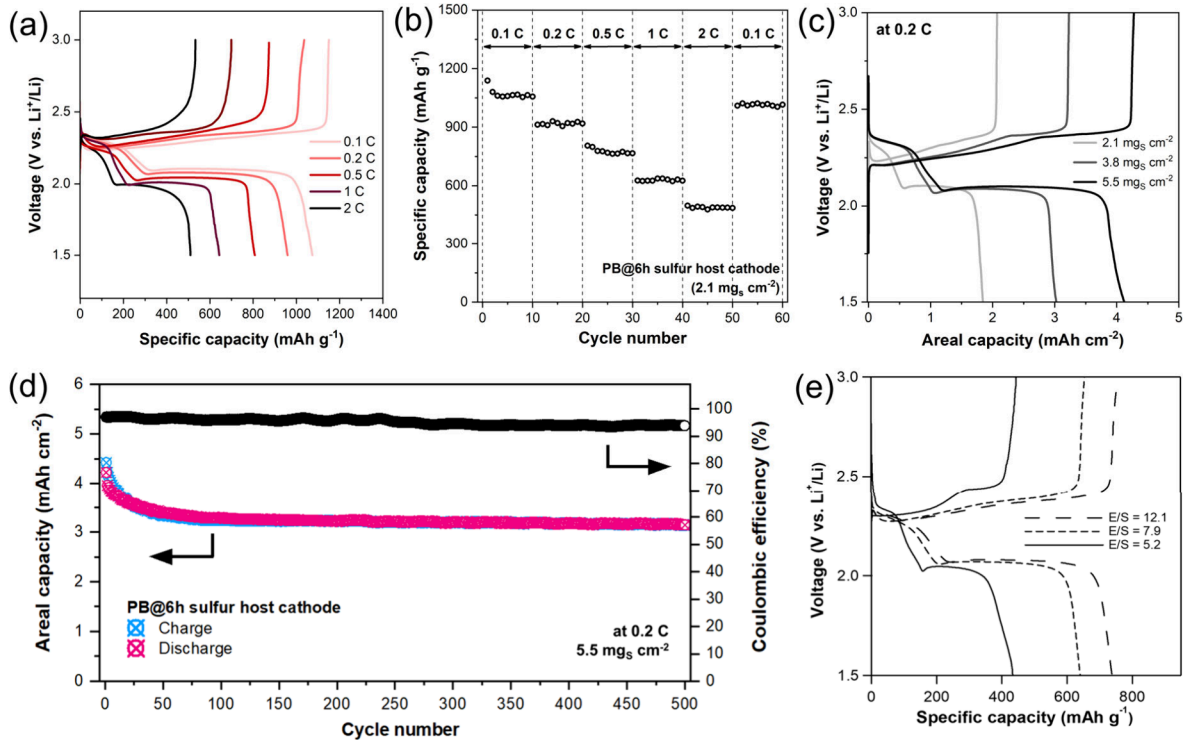

Figure 4. Battery performance of PB@6h sulfur host cathode. (a) Initial discharge−charge profiles at different C rates. (b) Cycle capacities at different C-rates. (c) Cyclic capacity of PB@6h electrode with sulfur loading of 5.5 mg_S cm^{-2} at 0.2 C for 500 cycles. (d) Charge−discharge profiles of PB@6h electrodes with varying sulfur loadings at 0.2 C. (e) Initial discharge−charge profiles of Li−S coin cell using PB@6h as the sulfur host material at various electrolyte-to-sulfur (E/S) ratios at 0.2 C.

without significant volumetric expansion or shrinkage, demonstrating excellent structural durability. The significant advantages of our structures are further demonstrated under lean-electrolyte conditions. The assembled Li−S batteries using PB@6h as a sulfur host material operate effectively across a range of E/S ratios from 12.1 to 5.2 (Figure 4e). A high specific capacity of 432 mAh g^{-1} at 0.2 C was achieved under lean electrolyte conditions (5.2 μL mg^{-1}) and a high sulfur loading (9.9 mg cm^{-2}). Under the same conditions, the cells retained 66.8% of their initial specific capacity after 50 cycles at 0.2 C (Figure S24a) and 60.6% after 100 cycles at 1 C (Figure S24b). This indicates that PB@6h significantly improves the slow kinetics and operational efficiency of the sulfur cathode. This underscores the clear advantages of the as-prepared frameworks in improving the electrochemical performance of Li−S batteries and enabling high sulfur utilization in lean-electrolyte environments. When comparing its performance, PB@6h has the potential to compete with commercial Li-ion batteries and outperforms previously reported sulfur host materials for Li−S batteries (Table S4). Furthermore, three Li−S coin cells using PB@6h powered a yellow LED, whereas PB@0.2h could not, highlighting PB@6h's superior performance as a sulfur host material (Figure S25).

Our research introduces highly porous concave nanocube structures of $CoFe_2O_4$, derived from a Prussian blue analogue, as effective sulfur host materials for high-performance Li−S batteries. We studied the impact of morphological changes, such as surface area and pore volume distribution, on Li^+ diffusion during charging and discharging. By measuring Li^+ diffusion coefficients using CV and GITT, we found that increased pore volume and surface area enhanced lithium polysulfide conversion and Li^+ diffusivity. *Operando* Raman spectroscopy confirmed that porosity defects on the catalyst surface lowered the reaction barriers, speeding up sulfur reduction. The optimized $CoFe_2O_4$ nanocubes (i.e., PB@6h) demonstrated outstanding cycling performance, with a minimal capacity fading rate of 0.05% per cycle at 2 C. It achieved a high capacity of 4.1 mAh cm^{-2} with a sulfur loading of 5.5 mg_S cm^{-2} and a specific capacity of 432 mAh g^{-1} at 0.2 C even with a low E/S ratio of 5.2. This performance surpasses that of conventional Li-ion batteries, highlighting the potential of porous defect engineering in sulfur host materials for advancing Li−S battery technology.

■ ASSOCIATED CONTENT

Supporting Information

The Supporting Information is available free of charge at https://pubs.acs.org/doi/10.1021/acsenergylett.4c02857.

Experimental details and materials characterizations and additional characterization and electrochemical test results of as-prepared Li−S coin cells using Prussian blue analogue series (PDF)

■ AUTHOR INFORMATION

Corresponding Author

Héctor D. Abruña − *Department of Chemistry and Chemical Biology, Cornell University, Ithaca, New York 14853, United States;* orcid.org/0000-0002-3948-356X; Email: hda1@cornell.edu

Authors

Dasol Jin − *Department of Chemistry and Chemical Biology, Cornell University, Ithaca, New York 14853, United States*

https://doi.org/10.1021/acsenergylett.4c02857
ACS Energy Lett. 2024, 9, 5822−5829

Mihail R. Krumov − *Department of Chemistry and Chemical Biology, Cornell University, Ithaca, New York 14853, United States*

Ruth M. Mandel − *Department of Chemistry and Chemical Biology, Cornell University, Ithaca, New York 14853, United States*

Phillip J. Milner − *Department of Chemistry and Chemical Biology, Cornell University, Ithaca, New York 14853, United States;* orcid.org/0000-0002-2618-013X

Complete contact information is available at: https://pubs.acs.org/10.1021/acsenergylett.4c02857

Notes

The authors declare no competing financial interest.

■ ACKNOWLEDGMENTS

The authors gratefully acknowledge support from the Abruña Energy Initiative, in the Department of Chemistry and Chemical Biology, College of Arts and Sciences, at Cornell University. This material is based upon work supported by the National Science Foundation under Grant No. CBET-2047627 (R.M.M., P.J.M.). Any opinions, findings, and conclusions or recommendations expressed in this material are those of the author(s) and do not necessarily reflect the views of the National Science Foundation. We acknowledge the support of a Camille Dreyfus Teacher-Scholar Award to P.J.M. (TC-23-048).

■ REFERENCES

(1) Zhao, M.; Li, B.-Q.; Zhang, X.-Q.; Huang, J.-Q.; Zhang, Q. A Perspective toward Practical Lithium-Sulfur Batteries. *ACS Cent. Sci.* **2020**, *6* (7), 1095−1104.

(2) Liu, J.; Bao, Z.; Cui, Y.; Dufek, E. J.; Goodenough, J. B.; Khalifah, P.; Li, Q.; Liaw, B. Y.; Liu, P.; Manthiram, A.; Meng, Y. S.; Subramanian, V. R.; Toney, M. F.; Viswanathan, V. V.; Whittingham, M. S.; Xiao, J.; Xu, W.; Yang, J. H.; Yang, X. Q.; Zhang, J. G. Pathways for Practical High-Energy Long-Cycling Lithium Metal Batteries. *Nat. Energy* **2019**, *4* (3), 180−186.

(3) Li, G.; Wang, S.; Zhang, Y.; Li, M.; Chen, Z.; Lu, J. Revisiting the Role of Polysulfides in Lithium-Sulfur Batteries. *Adv. Mater.* **2018**, *30* (22), 1705590.

(4) Zhang, Y.; Jiang, Y.; Bai, S.; Dong, Z.; Cao, X.; Wei, Q.; Wang, Y.; Zhang, Z.; Liu, Y. Ultra-Fast Uranium Capture via the Synergistic Interaction of the Intrinsic Sulfur Atoms and the Phosphoric Acid Groups Adhered to Edge Sulfur of MoS_2. *J. Hazard. Mater.* **2023**, *457*, 131745.

(5) Shen, L.; Song, Y.-W.; Wang, J.; Zhao, C.-X.; Bi, C.-X.; Sun, S.-Y.; Zhang, X.-Q.; Li, B.-Q.; Zhang, Q. Synergistic Catalysis on Dual-Atom Sites for High-Performance Lithium-Sulfur Batteries. *Small Struct.* **2023**, *4* (6), 2200205.

(6) Liu, Y.; Zhao, M.; Hou, L.-P.; Li, Z.; Bi, C.-X.; Chen, Z.-X.; Cheng, Q.; Zhang, X.-Q.; Li, B.-Q.; Kaskel, S.; Huang, J.-Q. An Organodiselenide Comediator to Facilitate Sulfur Redox Kinetics in Lithium-Sulfur Batteries with Encapsulating Lithium Polysulfide Electrolyte. *Angew. Chem., Int. Ed.* **2023**, *62* (30), e202303363.

(7) Zheng, M.; Chi, Y.; Hu, Q.; Tang, H.; Jiang, X.; Zhang, L.; Zhang, S.; Pang, H.; Xu, Q. Carbon Nanotube-Based Materials for Lithium-Sulfur Batteries. *J. Mater. Chem. A* **2019**, *7* (29), 17204−17241.

(8) Chen, Y.; Zou, K.; Dai, X.; Bai, H.; Zhang, S.; Zhou, T.; Li, C.; Liu, Y.; Pang, W. K.; Guo, Z. Polysulfide Filter and Dendrite Inhibitor: Highly Graphitized Wood Framework Inhibits Polysulfide Shuttle and Lithium Dendrites in Li-S Batteries. *Adv. Funct. Mater.* **2021**, *31* (31), 2102458.

(9) Duivenvoorden, T.; Sanderson, S.; Searles, D. J. Cathode Atomic Structures and Their Electrolyte Interfaces in Lithium-sulfur Batteries. *Batteries & Supercaps* **2024**, *7* (1), e202300324.

(10) Wang, L.; Song, Y.-H.; Zhang, B.-H.; Liu, Y.-T.; Wang, Z.-Y.; Li, G.-R.; Liu, S.; Gao, X.-P. Spherical Metal Oxides with High Tap Density as Sulfur Host to Enhance Cathode Volumetric Capacity for Lithium-Sulfur Battery. *ACS Appl. Mater. Interfaces* **2020**, *12* (5), 5909−5919.

(11) Palchoudhury, S.; Ramasamy, K.; Han, J.; Chen, P.; Gupta, A. Transition Metal Chalcogenides for Next-Generation Energy Storage. *Nanoscale Adv.* **2023**, *5* (10), 2724−2742.

(12) Zhang, W.; Li, Y.; Lv, H.; Xie, S.; Zhu, J.; Xu, J.; Jin, H.; Kong, X.; Jin, S.; Wang, H.; Wu, X.; Ji, H. A Comparison Study of the Electrocatalytic Sulfur Reduction Activity on Heteroatom-Doped Graphene for Li-S Battery. *Small Struct.* **2023**, *4* (3), 2200244.

(13) Li, Y.; Wu, H.; Wu, D.; Wei, H.; Guo, Y.; Chen, H.; Li, Z.; Wang, L.; Xiong, C.; Meng, Q.; Liu, H.; Chan, C. K. High-Density Oxygen Doping of Conductive Metal Sulfides for Better Polysulfide Trapping and Li_2S-S_8 Redox Kinetics in High Areal Capacity Lithium-Sulfur Batteries. *Adv. Sci.* **2022**, *9* (17), 2200840.

(14) Zhou, L.; Danilov, D. L.; Eichel, R.-A.; Notten, P. H. L. Host Materials Anchoring Polysulfides in Li-S Batteries Reviewed. *Adv. Energy Mater.* **2021**, *11* (15), 2001304.

(15) Zhou, C.; Hong, M.; Hu, N.; Yang, J.; Zhu, W.; Kong, L.; Li, M. Bi-Metallic Coupling-Induced Electronic-State Modulation of Metal Phosphides for Kinetics-Enhanced and Dendrite-Free Li-S Batteries. *Adv. Funct. Mater.* **2023**, *33* (14), 2213310.

(16) Zhang, Z.; Avdeev, M.; Chen, H.; Yin, W.; Kan, W. H.; He, G. Lithiated Prussian Blue Analogues as Positive Electrode Active Materials for Stable Non-Aqueous Lithium-Ion Batteries. *Nat. Commun.* **2022**, *13* (1), 7790.

(17) Seok, J.; Yu, S.-H.; Abruña, H. D. Operando Synchrotron-Based X-ray Study of Prussian Blue and Its Analogue as Cathode Materials for Sodium-Ion Batteries. *J. Phys. Chem. C* **2020**, *124* (30), 16332−16337.

(18) Du, M.; Shi, J.; Shi, Y.; Zhang, G.; Yan, Y.; Geng, P.; Tian, Z.; Pang, H. Effects of O, S, and P in Transition-Metal Compounds on the Adsorption and Catalytic Ability of Sulfur Cathodes in Lithium-Sulfur Batteries. *Chem. Sci.* **2024**, *15*, 9775−9783.

(19) Shen, N.; Li, T.; Li, B.; Wang, Y.; Liu, H.; Guo, C.; Chen, X.; Li, J. Dual-Functional Mediators of High-Entropy Prussian Blue Analogues for Lithiophilicity and Sulfiphilicity in Li-S Batteries. *Nanoscale* **2024**, *16*, 7634−7644.

(20) Gu, L.-L.; Gao, J.; Wang, C.; Qiu, S.-Y.; Wang, K.-X.; Gao, X.-T.; Sun, K.-N.; Zuo, P.-J.; Zhu, X.-D. Thin-Carbon-Layer-Enveloped Cobalt-Iron Oxide Nanocages as a High-Efficiency Sulfur Container for Li-S Batteries. *J. Mater. Chem. A* **2020**, *8*, 20604−20611.

(21) Maeng, H. J.; Kim, D.-H.; Kim, N.-W.; Ruh, H.; Lee, D. K.; Yu, H. Synthesis of Spherical Prussian Blue with High Surface Area Using Acid Etching. *Curr. Appl. Phys.* **2018**, *18*, S21−S27.

(22) Cho, Y.; Jang, M.; Sang Lee, K.; Lee, E.; Park, S. Y.; Piao, Y. The Quinone-Based Conjugated Microporous Polymer as an Effective Electrode Additive for Activated Graphene Host Material in Lithium-Sulfur Batteries. *Chem. Eng. J.* **2023**, *463*, 142422.

(23) Mitra, S.; Veluri, P. S.; Chakraborthy, A.; Petla, R. K. Electrochemical Properties of Spinel Cobalt Ferrite Nanoparticles with Sodium Alginate as Interactive Binder. *ChemElectroChem.* **2014**, *1* (6), 1068−1074.

(24) Liu, Y.; Qiao, Y.; Zhang, W.; Li, Z.; Ji, X.; Miao, L.; Yuan, L.; Hu, X.; Huang, Y. Sodium Storage in Na-Rich $Na_xFeFe(CN)_6$ Nanocubes. *Nano Energy* **2015**, *12*, 386−393.

(25) Xu, M.; You, J.; Du, C.; Yu, Z.; Cheng, S. Mesoporous Hollow $Fe_4[Fe(CN)_6)]_3$ Hierarchical Nanocrystal Architecture for Advanced Sodium-Ion Batteries. *Int. J. Electrochem. Sci.* **2024**, *19*, 100642.

(26) Liu, N.; Du, P.; Zhou, P.; Tanguturi, R. G.; Qi, Y.; Zhang, T.; Zhuang, C. Annealing Temperature Effects on the Cation Distribution in $CoFe_2O_4$ Nanofibers. *Appl. Surf. Sci.* **2020**, *532*, 147440.

(27) Lee, D.; Cho, C.-W.; Kim, J. W.; Bae, J.-S.; Yun, H.-J.; Lee, J.; Park, S. Effect of Oxygen Vacancies in the Magnetic Properties of the Amorphous $CoFe_2O_4$ Films. *J. Non Cryst. Solids* **2017**, *456*, 83−87.
(28) Bazylewski, P.; Boukhvalov, D. W.; Kukharenko, A. I.; Kurmaev, E. Z.; Hunt, A.; Moewes, A.; Lee, Y. H.; Cholakh, S. O.; Chang, G. S. The Characterization of Co-Nanoparticles Supported on Graphene. *RSC Adv.* **2015**, *5* (92), 75600−75606.
(29) Zhang, H.; Diao, J.; Ouyang, M.; Yadegari, H.; Mao, M.; Wang, M.; Henkelman, G.; Xie, F.; Riley, D. J. Heterostructured Core-Shell Ni-Co@Fe-Co Nanoboxes of Prussian Blue Analogues for Efficient Electrocatalytic Hydrogen Evolution from Alkaline Seawater. *ACS Catal.* **2023**, *13* (2), 1349−1358.
(30) Zhou, Z.; Zhang, Y.; Wang, Z.; Wei, W.; Tang, W.; Shi, J.; Xiong, R. Electronic Structure Studies of the Spinel $CoFe_2O_4$ by X-ray Photoelectron Spectroscopy. *Appl. Surf. Sci.* **2008**, *254* (21), 6972−6975.
(31) Wang, W. P.; Yang, H.; Xian, T.; Jiang, J. L. XPS and Magnetic Properties of $CoFe_2O_4$ Nanoparticles Synthesized by a Polyacrylamide Gel Route. *Mater. Trans.* **2012**, *53* (9), 1586−1589.
(32) Zhang, N.; Yang, Y.; Feng, X.; Yu, S.-H.; Seok, J.; Muller, D. A.; Abruña, H. D. Sulfur Encapsulation by MOF-Derived CoS_2 Embedded in Carbon Hosts for High-Performance Li-S Batteries. *J. Mater. Chem. A* **2019**, *7* (37), 21128−21139.
(33) Qiu, X.; Hua, Q.; Zheng, L.; Dai, Z. Study of the Discharge/Charge Process of Lithium-Sulfur Batteries by Electrochemical Impedance Spectroscopy. *RSC Adv.* **2020**, *10* (9), 5283−5293.
(34) Lang, S.; Colletta, M.; Krumov, M. R.; Seok, J.; Kourkoutis, L. F.; Wen, R.; Abruña, H. D. Multidimensional Visualization of the Dynamic Evolution of Li Metal via In Situ/Operando Methods. *Proc. Natl. Acad. Sci. U. S. A.* **2023**, *120* (7), e2220419120.
(35) Wang, B.; Wang, L.; Ding, D.; Zhai, Y.; Wang, F.; Jing, Z.; Yang, X.; Kong, Y.; Qian, Y.; Xu, L. Zinc-Assisted Cobalt Ditelluride Polyhedra Inducing Lattice Strain to Endow Efficient Adsorption-Catalysis for High-Energy Lithium-Sulfur Batteries. *Adv. Mater.* **2022**, *34*, 2204403.
(36) Zuo, X.; Zhen, M.; Liu, D.; Yu, H.; Feng, X.; Zhou, W.; Wang, H.; Zhang, Y. A Multifunctional Catalytic Interlayer for Propelling Solid-Solid Conversion Kinetics of Li_2S_2 to Li_2S in Lithium-Sulfur Batteries. *Adv. Funct. Mater.* **2023**, *33* (15), 2214206.
(37) Zhou, F.; Wang, R.; He, S.; Liu, X.; Liu, S.; Shao, H.; Liu, X.; Xiao, Z.; Liu, J. Defect-Rich Hierarchical Porous Mn-Doped CoP Hollow Microspheres Accelerate Polysulfide Conversion. *Adv. Funct. Mater.* **2023**, *33* (8), 2211124.
(38) Ji, Y.; Yang, K.; Liu, M.; Chen, S.; Liu, X.; Yang, B.; Wang, Z.; Huang, W.; Song, Z.; Xue, S.; Fu, Y.; Yang, L.; Miller, T. S.; Pan, F. PIM-1 as a Multifunctional Framework to Enable High-Performance Solid-State Lithium-Sulfur Batteries. *Adv. Funct. Mater.* **2021**, *31* (47), 2104830.
(39) Nitta, N.; Wu, F.; Lee, J. T.; Yushin, G. Li-Ion Battery Materials: Present and Future. *Mater. Today* **2015**, *18* (5), 252−264.
(40) Lama, F. L.; Marangon, V.; Caballero, Á.; Morales, J.; Hassoun, J. Diffusional Features of a Lithium-Sulfur Battery Exploiting Highly Microporous Activated Carbon. *ChemSusChem* **2023**, *16* (6), e202202095.
(41) Rui, X. H.; Yesibolati, N.; Li, S. R.; Yuan, C. C.; Chen, C. H. Determination of the Chemical Diffusion Coefficient of Li^+ in Intercalation-Type $Li_3V_2(PO_4)_3$ Anode Material. *Solid State Ion.* **2011**, *187* (1), 58−63.
(42) Kim, J.; Park, S.; Hwang, S.; Yoon, W.-S. Principles and Applications of Galvanostatic Intermittent Titration Technique for Lithium-ion Batteries. *J. Electrochem. Sci. Technol.* **2022**, *13* (1), 19−31.
(43) Lee, Y.-S.; Ryu, K.-S. Study of the Lithium Diffusion Properties and High Rate Performance of $TiNb_6O_{17}$ as an Anode in Lithium Secondary Battery. *Sci. Rep.* **2017**, *7* (1), 16617.
(44) Yuan, C.; Li, H.; Liu, G.; Zeng, P.; Mao, J.; Zhang, L. Dynamic Evolution of Electrocatalytic Materials for Li-S Batteries. *Mater. Chem. Front.* **2023**, *7* (17), 3543−3559.

https://doi.org/10.1021/acsenergylett.4c02857
ACS Energy Lett. 2024, 9, 5822−5829